

This is the author's peer reviewed, accepted manuscript. However, the online version of record will be different from this version once it has been copyedited and typeset.

PLEASE CITE THIS ARTICLE AS DOI: 10.1063/5.0038222

29 November 2024 02:28:26

Enhancing Positron Production using Front Surface Target Structures

S. Jiang,^{1, a)} A. Link,¹ D. Canning,² J. A. Fooks,³ P. A. Kempler,⁴ S. Kerr,¹ J. Kim,⁵ M. Krieger,² N. S. Lewis,⁶

R. Wallace,¹ G. J. Williams,¹ S. Yalamanchili,⁶ and H. Chen¹

¹⁾Lawrence Livermore National Laboratory, Livermore, California 94550, USA

²⁾Laboratory For Laser Energetics, Rochester, New York 14623, USA

³⁾General Atomics, San Diego, California 92121, USA

⁴⁾California Institute of Technology, Pasadena, California 91125, USA

⁵⁾Center for Energy Research, University of California San Diego, San Diego, California 92093, USA

⁶⁾California Institute of Technology, Pasadena, California 92093, USA

(Dated: 5 February 2021)

We report a target design which produced a substantial gain in relativistic electron-positron pair production using high-intensity lasers and targets with large-scale micro-structures on their surface. Comparing to an unstructured target, a selected Si microwire array target yielded a near 100% increase in the laser-to-positron conversion efficiency and produced a 10 MeV increase in the average emitted positron energy under nominally the same experimental conditions. We had established a multi-scale particle-in-cell simulation scheme to simulate both the laser absorption and the subsequent pair productions in a thick metal target. The experimental results are supported by the simulations demonstrating the performance increase is due to a higher conversion efficiency of laser energy into electrons with kinetic energies greater than 10 MeV due to enhanced direct laser acceleration of electrons enabled by the microwire array.

Producing a high-density, relativistic electron-positron pair plasma in the laboratory could significantly deepen the understanding of exotic astrophysical objects such as pulsars and quasars, but is extremely challenging^{1–5}. With the advances in high intensity laser technology, several methods for pair production have been either demonstrated or proposed, with different mechanisms dominating the physics in different regimes of laser intensity. For example, the Schwinger mechanism⁶ requires an extremely high intensity, above $\sim 10^{29}$ W/cm², for spontaneous pair creation from vacuum, whereas the Breit-Wheeler (BW) mechanism⁷ requires about 10^{24} W/cm² for avalanche-type discharge^{8,9}. These intensities are far beyond the capability of state-of-the-art lasers (up to 10^{22} W/cm²).

An alternative method is to inject laser produced high-energy electrons into high-Z target materials^{4,10–16}, with the electrostatic field of the nucleus involved in the pair production process releasing the constraint on the laser electric field intensity. If a thick converter target is used, positrons are mainly produced through the 3-step Bethe-Heitler (BH) process¹⁷. First, relativistic electrons are generated through a laser plasma interaction (LPI) at the front side of the target. These electrons then transport through the high-Z material and produce high-energy photons via Bremsstrahlung radiation. Propagation of the high-energy photons in the field of nucleus then creates electron-positron pairs. The key step is to transfer laser energy into enough high-energy (10s of MeV) electrons, for which, only a moderate intensity laser ($\sim 10^{20}$ W/cm²) is needed. Experiments using this type of setup have produced up to 10^{12} pairs/shot, which is the highest

yield reported to date by use of lasers.

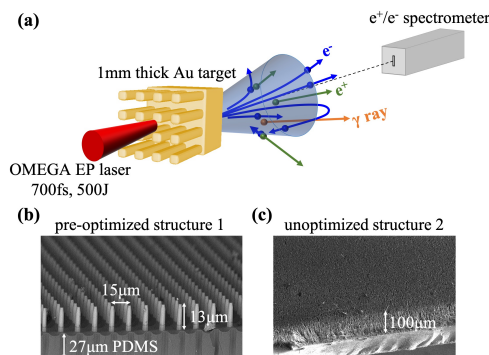


FIG. 1. (a) Schematic diagram of the experimental setup. (b) Scanning electron microscope (SEM) image of the pre-optimized target structure 1. (c) SEM image of the unoptimized structure 2.

A key to higher positron yield is the production of hotter electrons. Substantial enhancement in electron energies can be obtained by manipulating the laser-plasma interaction using a structured target^{18,19}. Specifically, highly-ordered silicon microwire arrays facing the laser pulse enable guiding the relativistic electron beam along the structured surface and moreover facilitate a direct laser acceleration mechanism. Such an electron beam can then create a substantial enhancement in the Bremsstrahlung radiation produced by a high-Z converter target²⁰. The Bremsstrahlung x-rays further interact with atomic nuclei and create more electron-positron pairs.

^{a)}Electronic mail: jiang8@llnl.gov

This is the author's peer reviewed, accepted manuscript. However, the online version of record will be different from this version once it has been copyedited and typeset.

PLEASE CITE THIS ARTICLE AS DOI: 10.1063/5.0038222

We demonstrate herein experimentally a substantial enhancement in both the yield and the energy of generated positrons using target structures, which suggests an efficient and inexpensive approach to improvement of positron sources. Particle-in-cell (PIC) simulations with the code Chicago²¹ have been used to explain the experimental results and have allowed a direct simulation of the LPI effects on the positron yield. Moreover, the simulation is in good qualitative agreement with the experimental data.

A schematic diagram of the experimental setup is shown in Figure 1(a). The structured target was irradiated with the OMEGA EP laser pulse, with a wavelength of $1.053\text{ }\mu\text{m}$, an energy of 500 J , and a pulse length of approximately 700 fs . 80% of the laser energy was enclosed in a $35\text{ }\mu\text{m}$ diameter focal spot as is derived from an on-shot waveform and far-field measurement. The peak intensity was estimated to be $4.5 \times 10^{20}\text{ W/cm}^2$ according to the measured fluence map. Prior to the experiment, the structure geometry (spacing and length) was optimized through PIC simulations of the hot electron temperature. This geometry, which we call structure 1, is an array of silicon microwires with $3\text{ }\mu\text{m}$ diameter, $13\text{ }\mu\text{m}$ length and $15\text{ }\mu\text{m}$ center-to-center transverse distance. For reference, we have also shot flat targets as well as another type of unoptimized structure (structure 2) that showed detrimental effects on electron energies in simulations. Structure 2 had $3\text{ }\mu\text{m}$ diameter, $100\text{ }\mu\text{m}$ length and $7\text{ }\mu\text{m}$ center-to-center distance. The microwires in the latter target had much longer lengths than the laser depth-of-focus, and much smaller space in between them than the laser focal spot size, so they tend to break the laser pulse during its propagation, resulting in a poor laser intensity at the critical density surface. Consequently they led to a low-energy electron spectrum.

Figure 1(b) and (c) show scanning electron microscope images of both target structures used in the experiment. The Si microwire arrays $100\text{ }\mu\text{m}$ in height (structure 2) were first grown on a $\text{Si} < 111 >$ wafer by the vapor-liquid-solid growth method²², whereas the shorter microwire arrays (structure 1) were etched from $\text{Si} < 100 >$ wafers via Deep Reactive Ion Etching²³. The microwires were then embedded in a $\sim 30\text{ }\mu\text{m}$ thick polydimethylsiloxane layer and peeled off of the substrate. This thin polydimethylsiloxane layer was then glued to a 1mm thick Au backing layer. In this case, the high-energy electrons generated and guided by the surface structures would transport through a thick high-Z material (Au) and induce pair production. The transverse size of the Au block used in the experiment was also 1mm . The laser was directed at normal incidence onto the target and the microwire arrays were oriented along the laser direction. This configuration has been shown in previous work to yield the highest enhancement of electron energy^{18,19}. The positron spectra were measured by an electron/positron spectrometer on the back side of the target along the laser direction (which was also the target normal direction).

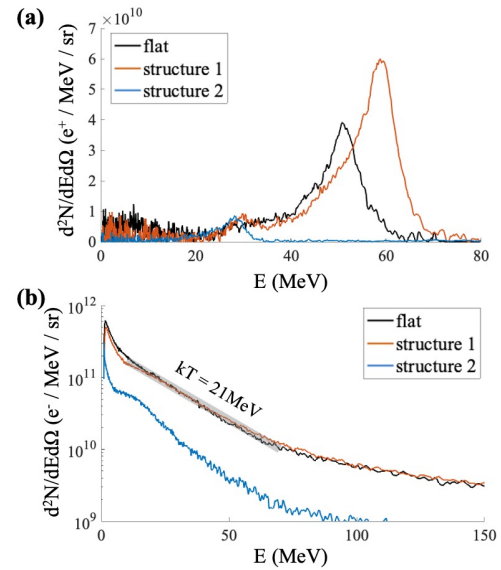


FIG. 2. Experimentally measured spectra for (a) positrons and (b) electrons. Different colors indicate the results from different targets under the same laser conditions.

The experimental positron and electron spectra for 3 different types of targets are shown in Figure 2(a) and (b). Target structure 1 generated about 50% more positrons than the regular flat target, and its laser to positron conversion efficiency increased by $\sim 97\%$ compared to the flat substrate. The spectrum peak also shifted from $\sim 50\text{ MeV}$ for the flat target to $\sim 60\text{ MeV}$ for structure 1. Structure 2 showed fewer as well as much lower-energy positrons, in accord with expectations as the length and spacing of the microwires encumber the laser focusing. The electron spectrum from structure 2 also showed the same trend, in agreement with the positron measurements. However, the electron spectra from flat and from structure 1 were mutually similar, with both having an electron temperature of about 21 MeV .

Multiple simulations to model the entire process were performed to elucidate why the measured positron spectrum from structure 1 is obviously superior while its electron spectrum is similar to that from flat target. The simulations used the same laser conditions and target geometries as the experiment. We fitted the measured laser fluence map with two Gaussian functions to maintain the intensity distribution of the experiment. The OMEGA EP laser had a substantial prepulse that could affect the conversion efficiency from the laser to fast electrons, and would therefore affect the yield and energy of positrons. The facility has an on-shot prepulse measurement from

This is the author's peer reviewed, accepted manuscript. However, the online version of record will be different from this version once it has been copyedited and typeset.

PLEASE CITE THIS ARTICLE AS DOI: 10.1063/5.0038222

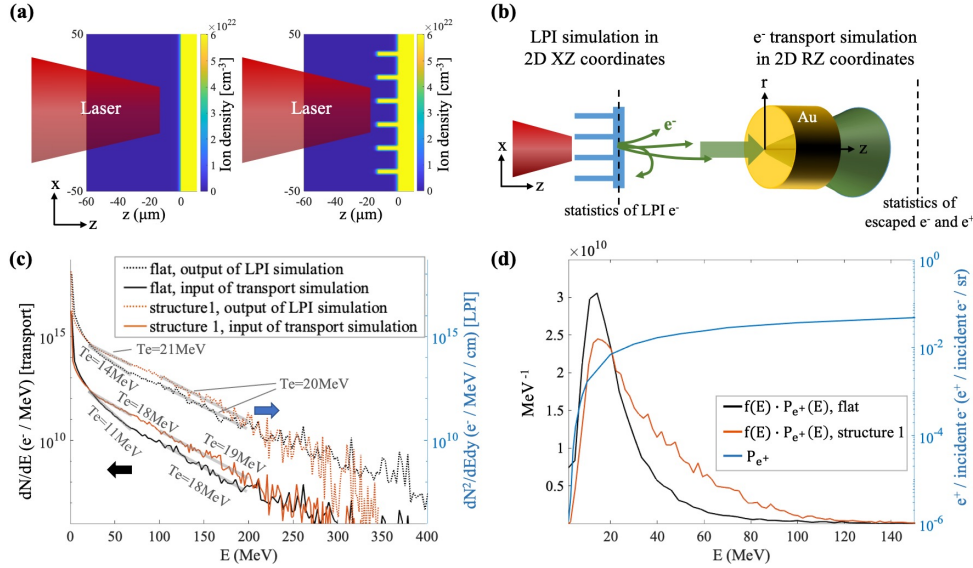


FIG. 3. (a) Initial ion density for 2D Cartesian LPI simulations. (b) Schematic diagram of simulation setups. We have injected the fast electrons derived from LPI simulation to the following transport simulation after converting the electron source from Cartesian to cylindrical geometry. (c) Electron spectra inside the target from 2D Cartesian LPI simulations (dashed curves, right y axis) and spectra of injected electron source for 2D cylindrical transport simulations (solid curves, left y axis). (d) Blue curve (right y axis) shows the probability of one positron generated by one 0° , monoenergetic electron transporting through a 1mm thick, 1mm diameter Au target, without considering any field effects. The black and red curves (with respect to the left y axis) show injection electron spectra multiplied by the positron generation probability as a function of energy.

ns to 1 ns prior to the main laser pulse. For the prepulse within 1 ns, we assumed a similar profile to that measured by Dorrer et al. on OMEGA EP²⁴. The total energy of the prepulse was about 3.5 mJ. Hydrodynamic simulations with the code HYDRA²⁵ were used to calculate the preplasma profile, as is shown in Figure 3(a). The preplasma scale length between relativistic critical density and critical density is about $2 \mu\text{m}$ and the scale length below critical density is $10 \mu\text{m}$.

Full 3D PIC simulations to model all physics processes are impractical with current supercomputers. We instead adopted a two-stage approach that has been demonstrated on other targets^{26,27} to simulate LPI and transport processes separately. Both stages were performed with the code Chicago²¹. The overall simulation process is illustrated in Figure 3(b). First a 2D Cartesian geometry was used to simulate the LPI process, with only x and z dimensions modeled in space. However, the velocity was 3D as all 3 components v_x , v_y and v_z were updated at each time step. We could not use a cylindrical geometry because the laser was linearly polarized in the x direction. The electrons were measured at a plane that was $5 \mu\text{m}$ inside the target. The energy, direction, position and time of each electron macroparticle have all

been recorded. We then processed the laser-generated electrons to get their distribution as a function of energy, angle, transverse distance, and time. At this point, we assumed a rotational symmetry along the laser propagation axis for both space and velocity, and converted the distribution to cylindrical coordinates. The transport simulation was performed in a 2D cylindrical geometry. When hot electrons leave the target, they would create a strong sheath field on the back side. It is critical to model the sheath field properly to obtain the correct yield and spectrum. The cylindrical geometry is required to accurately model the $1/r^2$ fall-off of the E field, whereas the 2D Cartesian geometry would result in a $1/r$ fall-off. The hot electrons were then re-sampled according to its distribution and injected into a 1mm thick, 1mm diameter Au target in a 2D cylindrical geometry. Positron generation and transport was then simulated both inside and behind the Au target. To compare with the experimental results, statistics of escaped electrons and positrons were performed at another extraction plane that was 2mm from the backside of the target.

The electron spectra generated from the LPI simulations are shown in Figure 3(c). The dashed curves are the raw distributions derived in Cartesian coordinates and

This is the author's peer reviewed, accepted manuscript. However, the online version of record will be different from this version once it has been copyedited and typeset.

PLEASE CITE THIS ARTICLE AS DOI: 10.1063/5.0038222

the solid curves are converted distributions in cylindrical coordinates. Note that the 2D Cartesian simulation has a virtual dimension in y axis so the electron spectrum has a different unit, corresponding to the right y axis in Figure 3(c). The electron temperatures T_e for different portions of the spectra are also labeled in the plot. After conversion, the temperature for higher-energy-range electrons is maintained at around 20 MeV, which is quite close to the experimentally measured temperature of 21 MeV. Lower energy electrons have a wider angular distribution and thus tend to be more easily affected by the conversion. T_e decreased by about 3 MeV for electrons within 25 – 70 MeV. Comparing structure 1 (red) to flat (black), the main difference appears at energies above 25 MeV, as structure 1 tends to produce about an order of magnitude more electrons within this energy range.

To evaluate the positron yield by different electron spectra, in Figure 3(d) we have plotted $f(E) \cdot P_{e^+}(E)$, where $f(E)$ is the spectrum of injected electrons (solid curves in Figure 3(c)), and $P_{e^+}(E)$ is the probability that one positron could be generated and exit from the 1mm thick, 1mm diameter Au target as one incident electron with energy E is normally injected. $P_{e^+}(E)$ (blue curve) was obtained using a Monte Carlo code MCNP²⁸ and the field effects have been ignored. Note that we cannot directly compare the positron yield from MCNP to the experimental result as the escaped positron yield and spectra is also largely affected by the self-generated field. MCNP only provides an estimation of the positron production capability of different energy electrons. The positron production probability grows sharply with energy for incident electrons below ~30 MeV and gradually saturates at high energies. The black and red solid curves indicate the calculated $f(E) \cdot P_{e^+}(E)$ for flat and structured targets, respectively. Both curves peak at about 15 MeV. However, electrons within 25 – 150 MeV from structure 1 contributed to a great extent to the positron yield, whereas for the flat target most of the positrons are generated by lower energy electrons. Overall, the injection spectrum from structure 1 produced about 30% more positrons than the flat target. Note that this estimation does not consider any field or electron reflux effects that in reality play an important role.

The Monte Carlo simulation only provides an intuitive view of the pair production capability of LPI electrons. Understanding the energy difference in the measured positron spectra requires closer evaluation of the transport PIC simulations that involve the sheath field. The comparison of modeled and experimentally measured positron spectra at target normal (laser direction) is shown in Figure 4(a). The simulated spectra agree qualitatively with the experimental data. In Figure 4(b), the dark solid curves show the simulated spectra of escaped electrons at 0° whereas for comparison the light solid curves in the background show the corresponding experimental spectra. Both spectra have a relatively good overlap within the energy range between 40 MeV and 110 MeV. At lower energy, the mismatch is expected

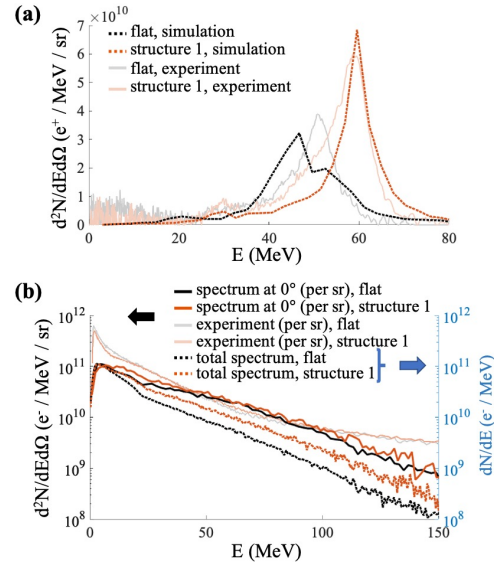


FIG. 4. (a) Positron spectra at 0° from simulations. (b) Electron spectra at 0° (solid lines, with unit $\text{MeV}^{-1}\text{sr}^{-1}$ on the left y axis) and overall electron spectra (dashed lines, with unit MeV^{-1} on the right y axis). Note that the two different spectra plotted have mutually different units. We have also plotted corresponding experimental spectra at 0° in the background for comparison.

because the experimentally measured spectra include electrons that are generated at much later times than those covered by the simulation. The simulated spectra showed less particles at high energies. However, according to Figure 3(d), electrons above 110 MeV would make a negligible contribution to the positron yield. These high energy electrons have a small impact on the sheath field as well because their total charge is low. Therefore, the simulated positron and electron spectra indicate that the injected electron source from LPI simulation models the experimental condition reasonably well. For both the flat and the structure 1 target, the electron spectra measured at the target normal direction are mutually quite similar, whereas the positron spectra are obviously different, in accord with experimental observations. In Figure 4(b) we have also plotted the total electron spectrum (in MeV^{-1}) as the dashed black and red curves. Unlike the spectra at 0°, the total spectrum from structure 1 clearly shows more high energy electrons, which explains the large discrepancy in the positron spectra, as forward going positrons are generated by all electrons, not just by the forward ones.

There are two acceleration mechanisms that are responsible for the highest energy electrons, including the loop-

This is the author's peer reviewed, accepted manuscript. However, the online version of record will be different from this version once it has been copyedited and typeset.

PLEASE CITE THIS ARTICLE AS DOI: 10.1063/5.0038222

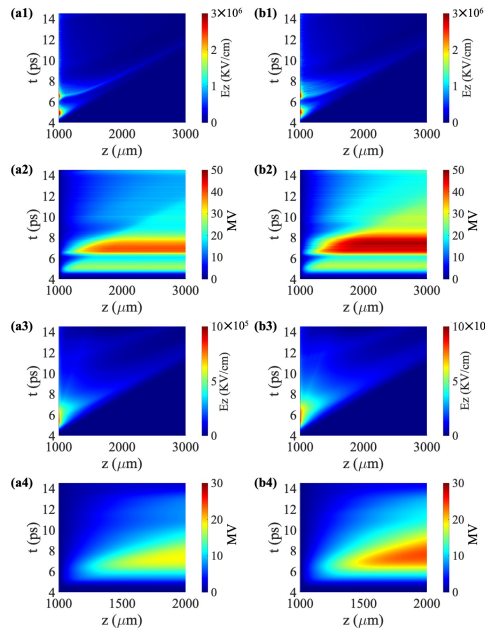


FIG. 5. (a1), (b1) Sheath field E_z at $r = 0$ as a function of time and longitudinal position z . (a2), (b2) corresponding voltage calculated by integrating E_z over z . (a3), (b3) Average E_z over the back surface of the target. (a4), (b4) corresponding voltage by integrating the average E_z . Here column (a) is for flat target and column (b) is for optimally structured target.

The energy of positrons is largely determined by the sheath field on the back side of the target. Figure 5 shows the evolution of the sheath field E_z as a function of the longitudinal position z and time t . Column (a) are the results from the flat target and column (b) are from structure 1. Images (a1),(b1) and (a3),(b3) show the E_z field at $r=0$ and average E_z field over the 1 mm diameter disk respectively, whereas (a2), (b2) and (a4), (b4) are the corresponding voltages V calculated by integrating E_z over the longitudinal distance z . $V = \int_{z_0}^z E_z dz$, where $z_0 = 1$ mm indicates the back surface of the target. These plots allow for an estimate of the accelerating capability

of the sheath field. The images at $r = 0$ indicate that passes of electrons gradually build up the sheath field on the target backside. Comparing the integrated voltage for flat and structured targets, both the voltage at $r = 0$ and the average voltage for the structured target are about 10 MV higher than that for flat target, which is consistent with the measured energy difference between their positron peaks.

The two-stage PIC simulation reproduced the experimental results, suggesting its potential for further target structure optimization to control the yield and energy of positrons and other secondary particles, such as ions that are also greatly influenced by the sheath field. Optimal target parameters will vary substantially with laser pulse length, intensity, focal spot size, and the amount of prepulse. As we have shown, for a given laser condition, the structures can be optimized by performing 2D Cartesian LPI simulations and converting the electron distributions to cylindrical coordinates. After the conversion, the hot electron temperature and the laser-to-electron conversion efficiency can both be realistic metrics for estimating the positron yield. We plan to probe a broader parameter space in future work.

In summary, front surface target structures have been shown experimentally to substantially enhance the positron yield and energy, constituting a cost-effective approach to use laser-generated positron sources for laboratory astrophysics applications. The follow-up simulations explain the entire process of how the laser-plasma interaction that is manipulated by the target structure affects the yield and energy of positrons. The agreement between the simulated and experimental spectra indicates the possibility of further target optimization using two-stage PIC simulations.

ACKNOWLEDGMENTS

We thank the OMEGA EP team for laser operation and technical support. This work was performed under the auspices of the U.S. DOE by LLNL under Contract DEAC5207NA27344, and funded by LDRD (#17ERD010). The fabrication of Si microwire arrays was supported through the Office of Science of the U.S. Department of Energy under Award No. DE-SC0004993. Additional support for this work was provided by the Lockheed Martin Corporation (Award 4103810021). We thank the staff at the Kavli Nanoscience Institute at Caltech for their technical assistance with fabrication.

DATA AVAILABILITY

The data that support the findings of this study are available from the corresponding author upon reasonable request.

This is the author's peer reviewed, accepted manuscript. However, the online version of record will be different from this version once it has been copyedited and typeset.

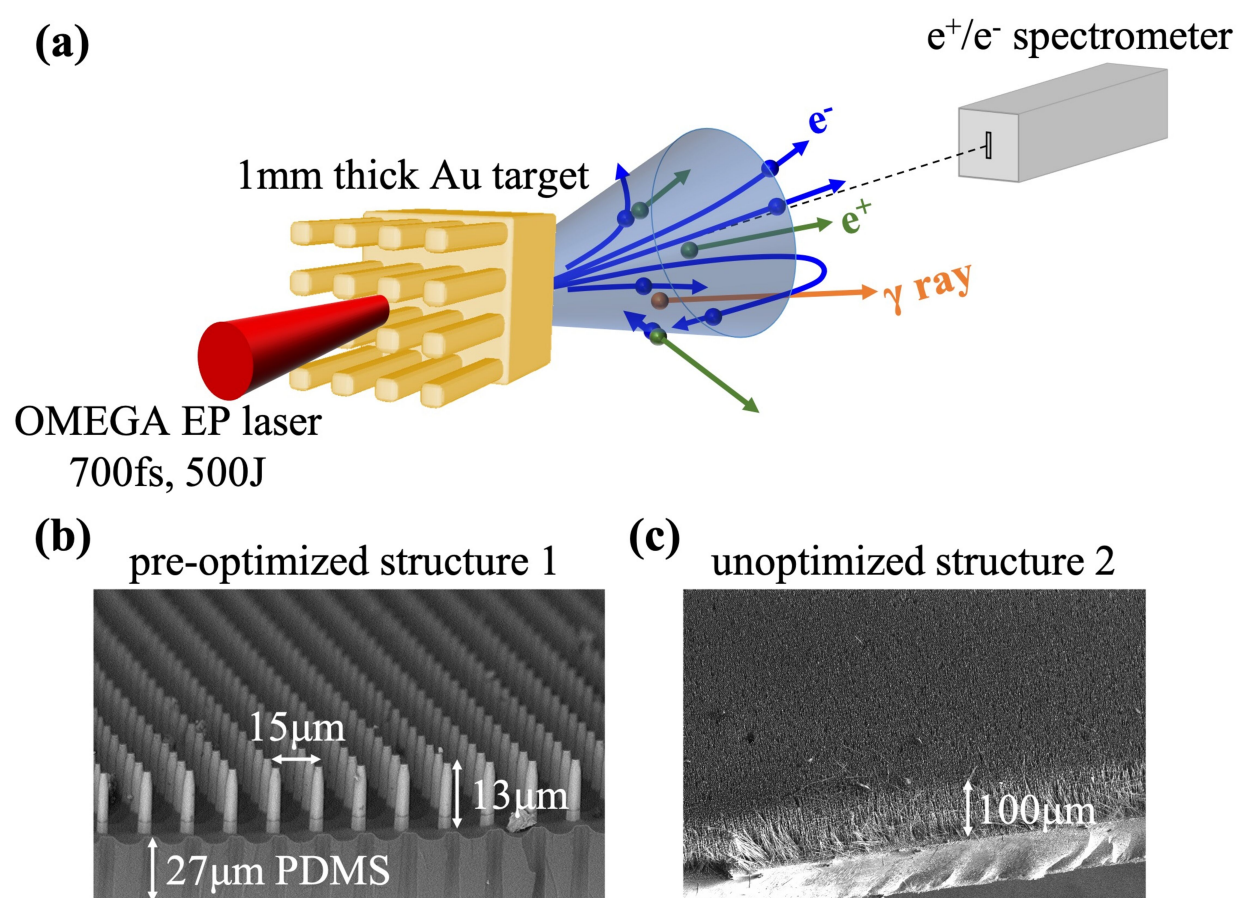
PLEASE CITE THIS ARTICLE AS DOI: 10.1063/5.0038222

6

- ¹T. Piran, Rev. Mod. Phys. **76**, 1143 (2005).
- ²H. Chen, D. D. Meyerhofer, S. C. Wilks, R. Cauble, F. Dollar, K. Falk, G. Gregori, A. Hazi, E. I. Moses, C. D. Murphy, *et al.*, High Energy Density Physics **7**, 225 (2011).
- ³E. Liang, T. Clarke, A. Henderson, W. Fu, W. Lo, D. Taylor, P. Chaguine, S. Zhou, Y. Hua, X. Cen, *et al.*, Sci. Report **5**, 13968 (2015).
- ⁴G. Sarri, K. Poder, J. M. Cole, W. Schumaker, A. D. Piazza, B. Reville, T. Dzelzainis, D. Doria, L. A. Gizzi, G. Grizzuti, *et al.*, Nat. Comm. **6**, 6747 (2015).
- ⁵M. Stoneking, T. S. Pedersen, P. Helander, E. V. Stenson, U. Hergenhahn, H. Saitoh, J. Horn-Stanja, J. R. Danielson, and C. M. Surko, "A new frontier in laboratory physics: electron-positron plasmas," To be published.
- ⁶J. Schwinger, Phys. Rev. **82**, 664 (1951).
- ⁷G. Breit and J. A. Wheeler, Phys. Rev. **46**, 1087 (1934).
- ⁸A. R. Bell and J. G. Kirk, Phys. Rev. Lett. **101**, 200403 (2008).
- ⁹C. P. Ridgers, C. S. Brady, R. Duclous, J. G. Kirk, K. Bennett, T. D. Arber, A. P. L. Robinson, and A. R. Bell, Phys. Rev. Lett. **165006**, 108 (2012).
- ¹⁰G. Sarri, W. Schumaker, A. D. Piazza, M. Vargas, B. Dromey, M. E. Dieckmann, V. Chvykov, A. Maksimchuk, V. Yanovsky, Z. H. He, *et al.*, Phys. Rev. Lett. **110**, 255002 (2003).
- ¹¹H. Chen, S. C. Wilks, D. D. Meyerhofer, J. Bonlie, C. D. Chen, S. N. Chen, C. Courtois, L. Elberson, G. Gregori, W. Krueer, *et al.*, Phys. Rev. Lett. **105**, 015003 (2010).
- ¹²H. Chen, G. Fiksel, D. Barnak, P.-Y. Chang, R. F. Heeter, A. Link, and D. D. Meyerhofer, Phys. Plasmas **21**, 040703 (2014).
- ¹³H. Chen, F. Fiuza, A. Link, A. Hazi, M. Hill, D. Hoarty, S. James, S. Kerr, D. D. Meyerhofer, J. Myatt, *et al.*, Phys. Rev. Lett. **114**, 215001 (2015).
- ¹⁴T. Xu, B. Shen, J. Xu, S. Li, Y. Yu, J. Li, X. Lu, C. Wang, X. Wang, X. Liang, *et al.*, Phys. Plasmas **23**, 033109 (2016).
- ¹⁵G. J. Williams, D. Barnak, G. Fiksel, A. Hazi, S. Kerr, C. Krauland, A. Link, M. J.-E. Manuel, S. R. Nagel, J. Park, *et al.*, Phys. Plasmas **23**, 123109 (2016).
- ¹⁶Y. Yan, Y. Wu, J. Chen, M. Yu, K. Dong, and Y. Gu, Plasma Phys. Control. Fusion **59**, 045015 (2017).
- ¹⁷H. Bethe and W. Heitler, Proc. Royal Soc. of London A **146**, 83 (1934).
- ¹⁸S. Jiang, L. Ji, H. Audesirk, K. George, J. Snyder, A. Krygier, P. Poole, C. Willis, R. Daskalova, E. Chowdhury, *et al.*, Phys. Rev. Lett. **116**, 085002 (2016).
- ¹⁹S. Jiang, A. G. Krygier, D. W. Schumacher, K. U. Akli, and R. R. Freeman, Phys. Rev. E **89**, 013106 (2014).
- ²⁰S. Jiang, A. G. Krygier, D. W. Schumacher, K. U. Akli, and R. R. Freeman, Eur. Phys. J. D **68**, 283 (2014).
- ²¹C. Thoma, D. R. Welch, R. E. Clark, D. V. Rose, and I. E. Golovkin, Phys. Plasmas **24**, 062707 (2017).
- ²²E. L. Warren, H. A. Atwater, and N. S. Lewis, J. Phys. Chem. C **118**, 747 (2014).
- ²³M. Henry, C. Welch, and A. Scherer, J. Vac. Sc. Technol. A **27**, 1211 (2009).
- ²⁴C. Dorner, A. Consentino, D. Irwin, J. Qiao, and J. D. Zuegel, J. Opt. **17**, 094007 (2015).
- ²⁵M. M. Marinak, G. D. Kerbel, N. A. Gentile, O. Jones, D. Munro, S. Pollaine, T. R. Dittrich, and S. W. Haan, Phys. Plasmas **8** (2001).
- ²⁶T. Bartal, M. E. Foord, C. Bellei, M. H. Key, K. A. Flippo, S. A. Gaillard, D. T. Offermann, P. K. Patel, L. C. Jarrott, D. P. Higginson, *et al.*, nature phys. **8**, 139 (2011).
- ²⁷H. Sawada, D. P. Higginson, A. Link, T. Ma, S. C. Wilks, H. S. McLean, F. Perez, P. K. Patel, and F. N. Beg, Phys. Plasmas **19**, 103108 (2012).
- ²⁸Los Alamos Scientific Laboratory. Group X-6. MCNP : a General Monte Carlo Code for Neutron and Photon Transport. Los Alamos, N.M. : [Springfield, Va.] :Dept. of Energy, Los Alamos Scientific Laboratory ; [for sale by the National Technical Information Service], 1979.
- ²⁹A. G. Krygier, D. W. Schumacher, and R. R. Freeman, Phys. Plasmas **21**, 023112 (2014).
- ³⁰Y. Sentoku, K. Mima, S. Kojima, and H. Ruhl, Phys. Plasmas **7**, 689 (2000).

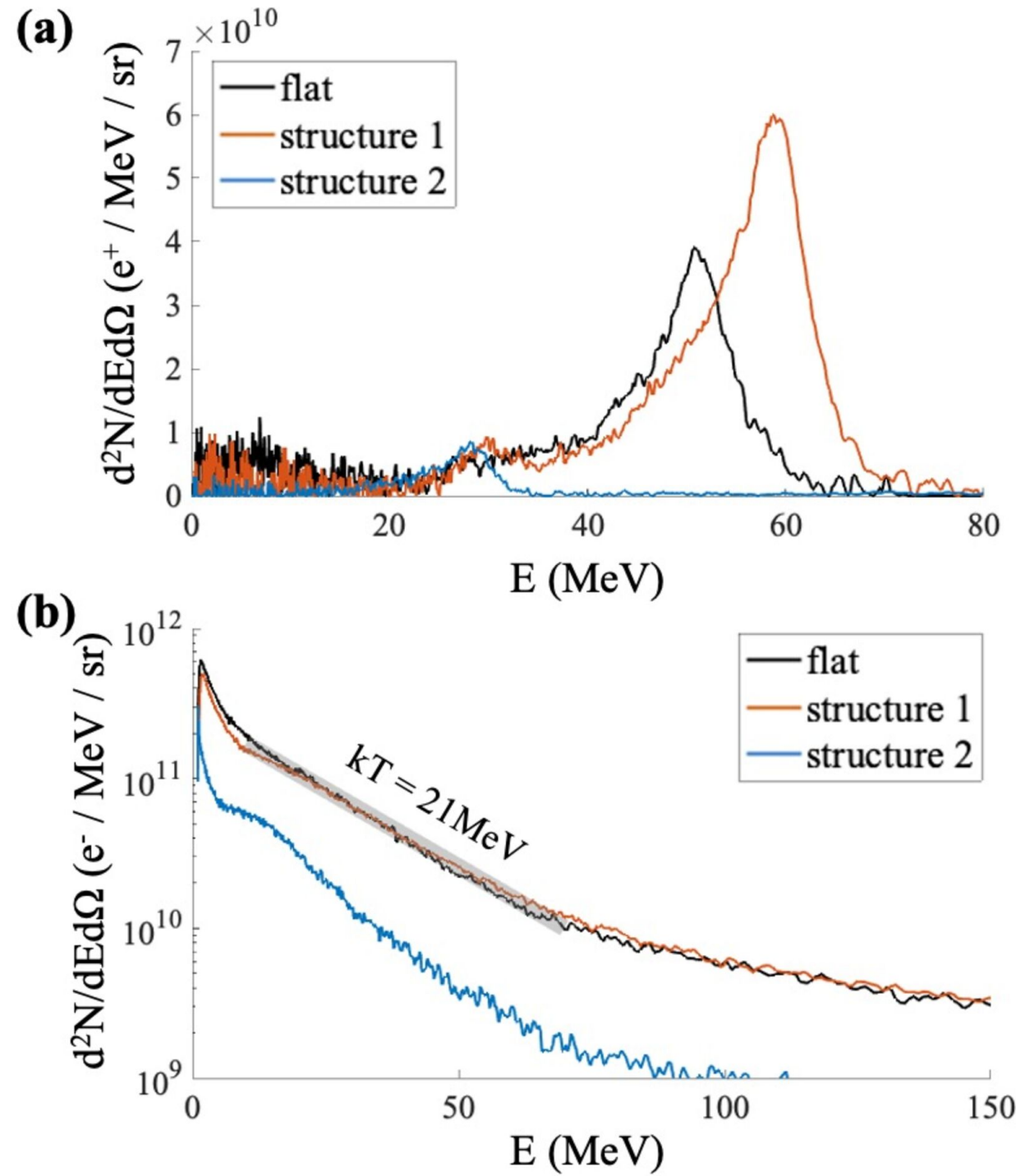
This is the author's peer reviewed, accepted manuscript. However, the online version of record will be different from this version once it has been copyedited and typeset.

PLEASE CITE THIS ARTICLE AS DOI: 10.1063/5.0038222



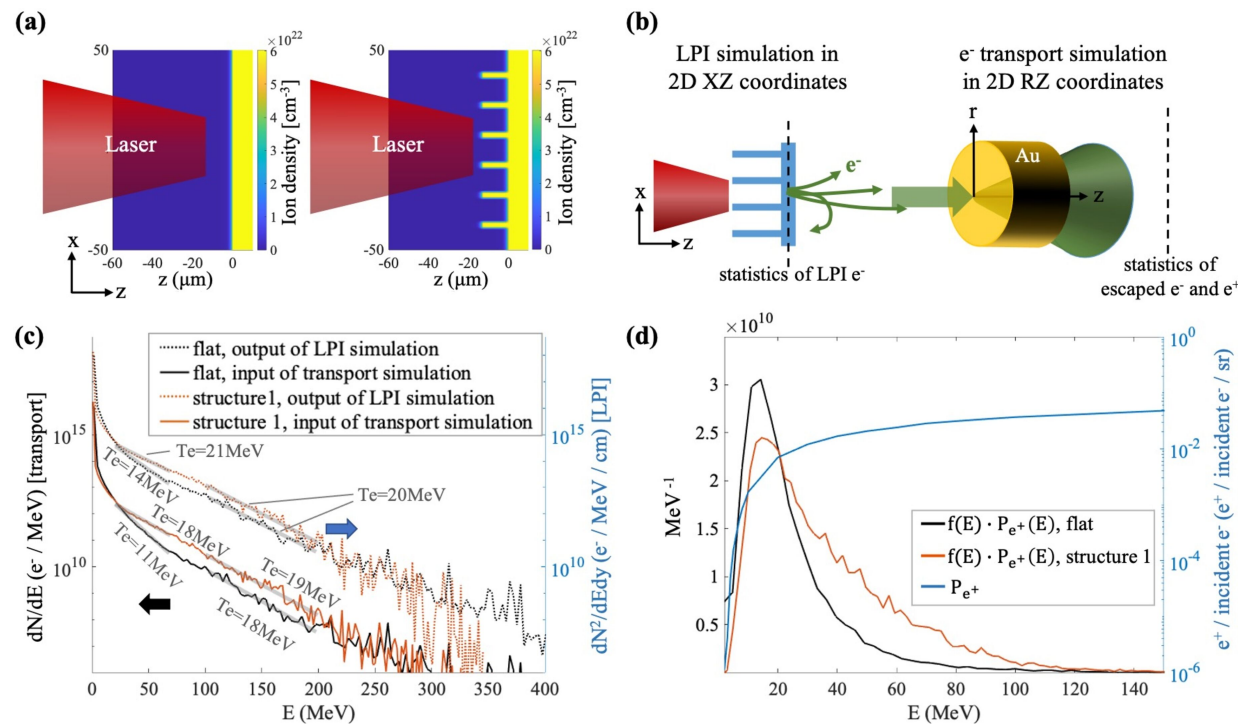
This is the author's peer reviewed, accepted manuscript. However, the online version of record will be different from this version once it has been copyedited and typeset.

PLEASE CITE THIS ARTICLE AS DOI: 10.1063/5.0038222



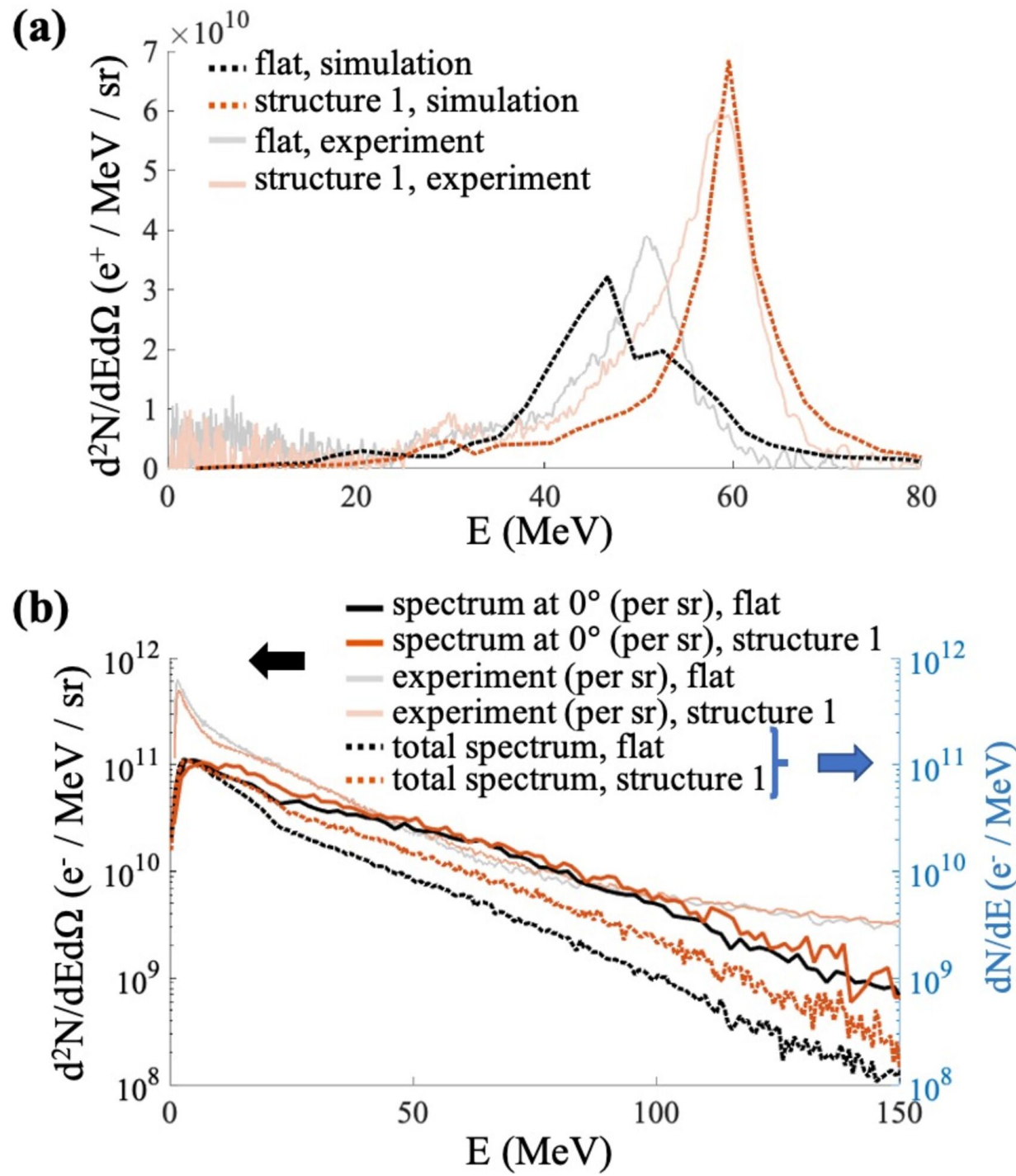
This is the author's peer reviewed, accepted manuscript. However, the online version of record will be different from this version once it has been copyedited and typeset.

PLEASE CITE THIS ARTICLE AS DOI: 10.1063/5.0038222



This is the author's peer reviewed, accepted manuscript. However, the online version of record will be different from this version once it has been copyedited and typeset.

PLEASE CITE THIS ARTICLE AS DOI: 10.1063/5.0038222





This is the author's peer reviewed, accepted manuscript. However, the online version of record will be different from this version once it has been copyedited and typeset.

PLEASE CITE THIS ARTICLE AS DOI: 10.1063/5.0038222

